Univerzita Komenského v Bratislave

Fakulta matematiky, fyziky a informatiky

Ashin Shaji

Autoreferát dizertačnej práce

Štúdium rastu tenkého filmu prostredníctvom in-situ röntgenového rozptylu

na získanie akademického titulu philosophiae doctor

v odbore doktorandského štúdia:

4.1.4. Kvantová elektronika a optika

Miesto a dátum:

Bratislava, 2021

Dizertačná práca bola vypracovaná v dennej forme doktorandského štúdia

na Fyzikálnom ústave Slovenskej akadémie vied

Predkladateľ: **Ashin Shaji**

Fyzikálny ústav, SAV

Dúbravská cesta 9

845 11 Bratislava

Školiteľ: **Dr. rer. nat. Peter Šiffalovič, DrSc.**

Fyzikálny ústav SAV

Fyzika 4.1.4. Kvantová elektronika a optika

(študijný odbor) (názov študijného programu doktorandského štúdia)

Predseda odborovej komisie:

....

(meno a priezvisko s uvedením titulov a hodností

a presná adresa jeho zamestnávateľa)

Abstrakt

Vykonala sa komplexná štúdia rastu tenkého filmu na 2D materiáloch pomocou röntgenového rozptylu in-situ, aby sa pochopili základné mechanizmy počas procesu rastu tenkého filmu. Táto práca sa zameriava hlavne na monitorovanie rastu tenkého filmu v reálnom čase pomocou in-situ meraní malouhlového rozptylu röntgenového žiarenia v reflexnej geometrii (GISAXS) a širokouhlého rozptylu röntgenového žiarenia v reflexnej geometrii (GIWAXS) s použitím na mieru yyhotovených experimentálnych zariadení. V prvej časti bola v laboratórnych podmienkach pomocou techniky GISAXS vykonaná in-situ štúdia sledovania samo-usporiadania pravidelnej štruktúry 3D Ge kvantových bodiek (QD) v amorfnej Al_2O_3 matrici počas depozície naprašovaním iónoým zväzkom periodickej viacvrstvovej Ge / Al_2O_3 štruktúry na kremíkový substrát. V závislosti na rýchlej repetitívnej akvizícii GISAXS máp, časový vývoj rastu 3D Ge QD štruktúry bol vyšetrovaný od dvojvrstvy k dvojvrstve za účelom určenia jej kryštalografického usporiadania, vertikálnych a laterálnych korelačných dĺžok, vzdialenosti medzi QD, atď. Zistilo sa, že 3D QD štruktúra má priestorovo centrovanú tetragonálnu mriežku s motívom uloženia ABA. Mriežkové parametre boli potvrdené fitovaním konečných GIWAXS máp založenom na parakryštalickom modeli. Výsledky simulácie naznačujú, že samousporiadanie Ge QD je od samého začiatku riadené iba morfológiou povrchu počas rastu. Ex-situ GISAXS meranie a meranie röntgenovskej reflektivity spolu s vysokorozlišovacou transmisnou elektrónovou mikroskopiou kompletizujú analýzu prezentovanú v tejto práci.

Druhá časť je zameraná na sledovanie rastu tenkej vrstvy MoS_2 na zafíre. MoS_2 je 2D materiál rodiny TMD so sľubnými výsledkami v aplikačnej rovine. Niektoré z jedinečných optických, elektronických a katalytických vlastností niekoľkovrstvových filmov MoS_2 vyplývajú zo špecifickej orientácie MoS_2 kryštálov v tenkej vrstve. Rast horizontálneho alebo vertikálne usporiadaného MoS_2 počas sulfurizácie vopred nadeponovanej Mo vrstvy je možné riadiť rôznymi fyzikálnymi podmienkami. V tejto práci prezentujeme komplexnú štúdiu uskutočňovanú v reálnom čase rastu niekoľkovrstvových MoS_2 filmov získaných sulfurizáciou Mo filmov pomocou in-situ GIWAXS techniky. Podarilo sa nám dokázať, že tok procesného plynu, ktorý ovplyvňuje parciálny tlak pár síry, je kľúčovým riadiacim parametrom pre orientáciu niekoľkovrstvovej vrstvy MoS_2, keď všetky ostatné parametre procesu zostávajú nezmenené. Sledovanie kryštalizácie niekoľkovrstvových vrstiev MoS_2 v reálnom čase nám umožnilo odhadnúť aktivačnú energiu potrebnú pre horizontálnu aj vertikálnu orientáciu.

Spolu s týmito výsledkami, nedávny a nepublikovaný výsledok sulfurizácie MoO_3 je tiež pridaný k výsledkom prezentovanými v tejto práci.

Abstract

A comprehensive study of thin film growth on 2D materials by *in-situ* X-ray scattering was performed to understand the underlying mechanisms during a thin film growth process. This work mainly focuses on the real-time monitoring of thin film growth formations using *in-situ* grazing-incidence small-angle X-ray scattering (GISAXS) and grazing-incidence wide-angle X-ray scattering (GIWAXS) measurements by implementing custom-designed experiment setups. A laboratory *in-situ* GISAXS tracking the self-assembled growth of a regular 3D Ge quantum dot (QD) structure in an Al_2O_3 amorphous matrix during the ion beam sputter deposition of a periodic Ge/Al_2O_3 multilayer on silicon is studied in the first part. Depending on a fast repetitive acquisition of GISAXS patterns, the temporal growth evolution of the 3D Ge QD structure was investigated bilayer by bilayer to determine its type, vertical and lateral correlation lengths, and inter-QD distance, etc. The QD structure was found to have a body-centered tetragonal lattice type with stacking type ABA. The lattice parameters were reassured by fitting the final GISAXS pattern depending on a paracrystal model. The simulation results suggest that the Ge QD self-assembly is controlled from the very beginning only by the growing surface morphology. *Ex-situ* GISAXS and X-ray reflectivity measurements along with a cross-section high-resolution transmission electron microscopy analysis complete the analysis.

The second part is focused on the monitoring of MoS_2 thin layer growth on sapphire. MoS_2 is a 2D material of the TMD family with promising application results. Some of the unique optical, electronic, and catalytical properties of few-layer MoS_2 films arise from its specific layer orientation. The growth of horizontally or vertically aligned MoS_2 during the sulfurization of pre-deposited Mo film can be controlled by various physical conditions. We perform a comprehensive real-time study of the growth of few-layer MoS_2 films by sulfurization of Mo films using *in-situ* GIWAXS. We prove that the process gas flow, which influences the sulfur partial vapor pressure, is the key parameter of control for the few-layer MoS_2 layer orientation when all other process parameters remain fixed. Tracking the crystallization of few-layer MoS_2 layers in real-time allowed us to estimate the activation energy required for both horizontal and vertical orientations. Along with it, the recent and unpublished result from the sulfurization of MoO_3 is also added to the results.

Contents

1 Introduction ... 5
2 Aim of the work ... 7
3 Measurement methods ... 8
3.1 Grazing-incidence small-angle X-ray scattering ... 8
3.2 Grazing incidence wide-angle X-ray scattering (GIWAXS) ... 8
3.3 In-situ GISAXS and GIWAXS ... 9
4 Experimental Section ... 11
4.1 In-situ GISAXS tracking of 3D Ge QDs structure ... 11
4.2 In-situ GIWAXS study of few-layer MoS_2 ... 12
5 Results and Discussion ... 16
5.1 In-situ GISAXS tracking of 3D Ge QDs structure ... 16
5.1.1 Temporal analysis layer by layer ... 16
5.2 In-situ GIWAXS study of few-layer MoS_2 films ... 20
5.2.1 *In-situ* Synchrotron GIWAXS measurements ... 20
5.2.2 Laboratory based *in-situ* GIWAXS measurements ... 25
6 Conclusion ... 28
7 List of author's publications ... 30
8 Bibliography ... 32

1 Introduction

Artificially fabricated structures with atomic precision such as layer-by-layer or atom-by-atom deposited thin films find their potential applications in the ever-growing electronics market. These important developments achieved in thin film fabrication initiated a fast development in size reduction of electronic devices [1]. The most noticeable works came out of the research on two-dimensional thin films and multilayers [2]. In my dissertation work, the first part of the thesis is devoted to the study of multilayered thin films, whereas the second part of the thesis is dedicated to the study of 2D thin films.

Thin films with multilayered structures always exhibit new physical phenomena, which are not occurring in the bulks or monolayer thin films. Properties like 2D-3D crossover effects in electron transport, magnetism or giant magnetoresistance are some of them. All these properties depend not only on the multilayer design in terms of the layer thickness, but also on the interface quality. Artificial multilayers are produced by alternating deposition of two or more compounds or elements on a solid substrate [3]. Multilayers are promising samples for interface physics as the interface phenomena are multiplicated. Therefore, interface studies using X-rays have a great importance for the analysis of multilayer structures. As a result, the interest in nanostructures that can assemble themselves became major field of research. Self-assembly has already proven to be an efficient method for fabricating quantum dot (QDs) arrays, since the islands can be unexpectedly uniform in size [4].

Multilayered structures play a crucial role in the production of quantum dots ordered with high spatial density, also known as the QD superlattices. The interesting feature of such structures is that the QDs (buried islands) in successive layers are spatially correlated. On the surface of each layer, new islands tend to nucleate directly above buried islands [5]. This spatial ordering arises from the strain at the surface due to buried strained islands. The deposition techniques employed for the fabrication of multilayers include various chemical and physical deposition methods. Ion-beam deposition became established technology for optics fabrication and is known to produce the smoothest layers with the highest material density approaching the bulk values. The Grazing-Incidence Small-Angle X-ray Scattering (GISAXS) is an established method for tracking and studying nanostructured surfaces and thin films [6,7]. The GISAXS technique can be implemented into an experiment as *in-situ* or *ex-situ* method. The advantage of *in-situ* GISAXS over *ex-situ* is the real-time layer-by-layer growth study of multilayer formation. So, the implementation of *in-situ* GISAXS together with ion-beam

deposition for the fabrication of QDs in multilayers is one of the main topics of interest of my thesis discussed in the first part.

Transition metal dichalcogenide (TMD) [8] materials that are semiconductors in nature are promising alternatives for graphene. The existence of vdW forces between the weakly bound 2D molecular layer makes the TMDs different from their bulk counterparts. Due to the unique electrical, optical and catalytic properties, MoS_2 is one of the most studied materials in the TMD family. The presence of strong ionic bonding in MoS_2 between the Mo and S atoms along with the presence of weak vdW force between various layers of MoS_2 is the reason behind its thickness-dependent bandgap, thermal and optical properties. Various methods are available for the production of monolayer or few-layer of MoS_2, such as exfoliation of bulk crystals, pulsed laser deposition or chemical vapor deposition (CVD), etc.

TMD materials with hexagonal close-packed structure like MoS_2 can grow with horizontal (HA) or vertical (VA) alignment on the substrate, depending on the fabrication conditions. HA MoS_2 layers are extensively used in the field of electronics and optoelectronics [9]. VA MoS_2 layers are gaining attention due to their chemically reactive edges, which are used for water disinfection, solar cells, water splitting and hydrogen evolution reactions (HER). The spatial orientation of the MoS_2 layers is crucial and determines its applications [10]. Hence, precise control over the growth orientations of such 2D TMD materials is critical to enhance their desired device functionalities and material properties. Since now, GIWAXS studies were performed only in *ex-situ* mode to study the orientation of MoS_2 layer. As in the case mentioned above for the *in-situ* GISAXS study of multilayers, an *in-situ* GIWAXS will help to unleash the hidden factors behind the crystal orientation of few-layer MoS_2 during its formation itself. So, the second part of this thesis is dedicated to the *in-situ* GIWAXS study of few-layer MoS_2 thin films in a custom build CVD reactor and also the first *in-situ* GIWAXS study of sulfurization of MoO_3 to MoS_2 in the laboratory.

2 Aim of the work

The main objective of the thesis can be divided into two sections based on the nature of the performed experiments. The first section is devoted to the research and devolvement of *in-situ* GISAXS analysis of multilayered thin films during its growth process.

The main objectives for the first set of experiments are:

- Setup the custom build dual-ion beam sputtering apparatus with *in-situ* GISAXS and optimization of the deposition process.
- Fabrication of 3D QD superlattices using multilayer deposition.
- *In-situ* real-time GISAXS study of Ge 3D QD structure formation and its ordering in Al_2O_3 amorphous matrix.
- Experimental verification of the influence of deposition temperature on the regularity of QD ordering.

The second section is devoted to the research and development for *in-situ* GIWAXS analysis of few- or monolayer of MoS_2 thin films in a custom-build CVD reactor.

The main objectives for the second set of experiments are:

- The development of laboratory/synchrotron beamline compatible CVD system with *in-situ* GIWAXS setup for measurements on 2D thin films.
- To execute a real-time study of the growth of few-layer MoS_2 films by sulfurization of Mo films using *in-situ* GIWAXS.
- To perform a study on the influence of sulfur partial vapor pressure on few-layer MoS_2 layer orientation. The aim is to estimate its effect on MoS_2 crystal formation and the activation energy required for both HA and VA orientations.
- The detailed testing of a developed device with a microfocus X-ray source (IμS, Incoatec) and 2D X-ray detector (Pilatus 100K and 200K, Dectris) in the laboratory. The aim is to examine the sulfurization process of Mo thoroughly and also to extend the possibilities of the system by testing different sets of materials such as MoO_3.

3 Measurement methods

3.1 Grazing-incidence small-angle X-ray scattering

Grazing-Incidence Small-Angle X-Ray Scattering (GISAXS) technique is a powerful tool to analyze the distribution and morphology of either islands on a substrate or buried particles [11]. It provides average information on electronic density variations at the nanoscale in addition to the grazing-incidence wide-angle X-ray scattering (GIWAXS) counterpart. For incidence angles near the angle of total external reflection of X-rays, the penetration depth of the wavefield is decreased to a few nanometers that enhances X-ray scattering from the near-surface regions compared to the bulk. Any deviation in the local electron density (islands, inclusions, surface roughness, particles, clusters, etc.) scatters either the reflected or the transmitted beam. Considering the distances on the order of nanometers covered by GISAXS analysis, the scattering intensity is collected close to the origin of the reciprocal space around the specularly reflected beam at small angles. GISAXS offers many advantages over conventional microscopes methods, since it offers an average value of the structure parameters inside the illuminated samples. It is a non-invasive technique at variance to transmission electron microscopy (TEM). Since it relies on X-ray photons scattering-, even the analysis of charged samples can be performed. GISAXS analysis can be implemented not only for the surface characterization, but also for the buried structures. Because of these properties, GISAXS technique can be used *in-situ* to monitor time-dependent changes in the morphology of thin films from ultra-high vacuum to gas or vapor atmospheres.

3.2 Grazing incidence wide-angle X-ray scattering (GIWAXS)

In contrast to GISAXS, GIWAXS records scattering patterns at large diffraction angles, i.e. it provides information about the atomic structure of crystalline materials [12]. Similar to GISAXS, GIWAXS method also evolved as an analytical tool for thin films and other soft matter materials due to its reduced probing volume. Instead of an incident beam at a 90° incident angle (transmission), a very low incident angle $\propto_i$ is applied in GIWAXS experiments. At such a low angle of incidence, the beam travels a notable long path inside the thin film via the footprint effect, allowing for the required scattering interaction to occur. GIWAXS is the analog of WAXS in reflection geometry, similar to how SAXS is to GISAXS. GIWAXS uses

the same principles of analysis and evaluation as GISAXS, but at large scattering angles. GIWAXS and GISAXS depending on the detector position, which is far away or close to the sample (shown in Figure 3.1). By these arrangements, a smaller or larger scattering angular range of scattered X-rays is covered by GISAXS or GIWAXS, respectively. Hence this method requires samples to be more crystalline or ordered for information to be extracted. Typically, the GISAXS encodes the length scales in the range of 1–1000 nm, while GIWAXS in 0.1–1 nm range.

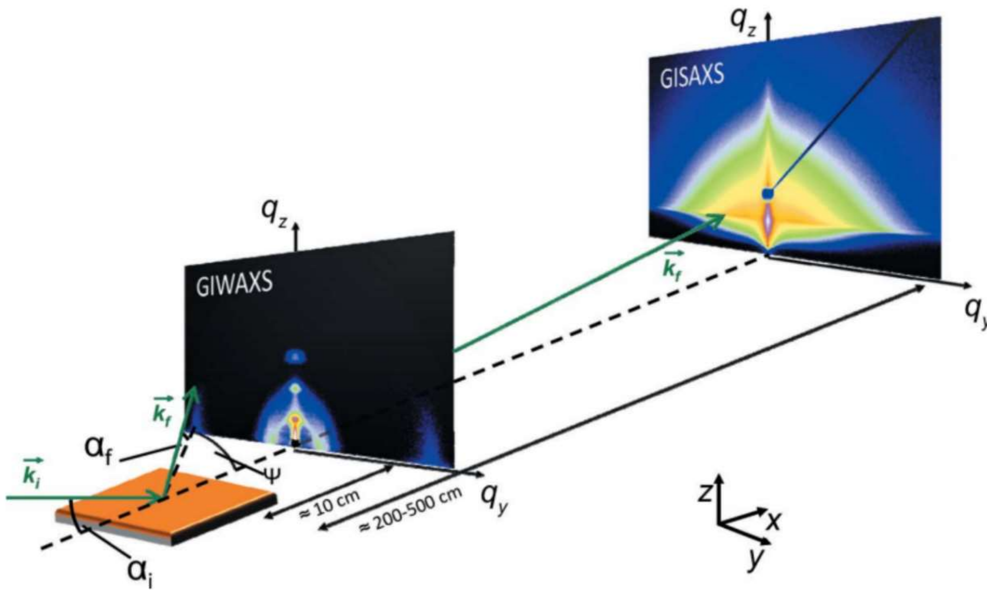

Figure 3.1 Graphical representation of the scattering geometry used in GISAXS and GIWAXS. Typical sample-to-detector distances difference for GIWAXS and GISAXS are shown [13].

3.3 In-situ GISAXS and GIWAXS

Kinetic information, which means the time-dependent evolution of characteristic properties of materials, has received very strong attention and is typically addressed with *in-situ* GISAXS and GIWAXS measurements. Among the various *in-situ* GISAXS and *in-situ* GIWAXS experiments, one major field of research follows the evolution of structure during film fabrication. In such experiments, the soft-matter film is deposited using techniques such as doctor blading, drop casting, spin coating, spray coating, printing, vacuum deposition or other types of deposition methods and the scattering experiment is performed in *in-situ* mode

during the deposition. Another established area of research is to follow structural transformations in soft-matter films during a post-production treatment after deposition. The most popular post-production treatments are vapor and/or thermal annealing.

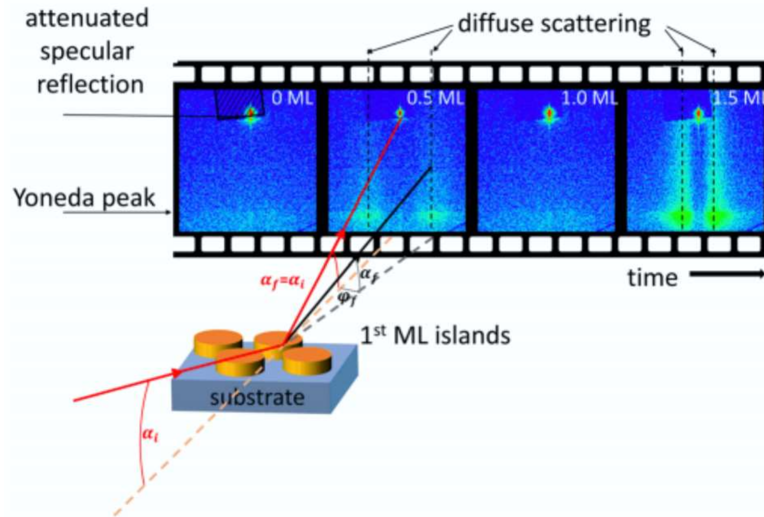

Figure 3.2 Schematics of an *in-situ* GISAXS geometry. The real-time diffuse scattering is recorded by using an area detector. Both the specular reflection (incidence angle α_i = exit angle α_f) and diffuse scattering can be monitored in such a setup [14].

Tracking down the structural evolution during deposition is demanding due to the fast processes involved, which in turn involve very short data acquisition times. Additionally, special equipment needs to be developed since most commercial deposition systems cannot be easily integrated into a synchrotron radiation instrument or beam line. By the ongoing advancement in instrumentation development, ultra-short counting times (in the order of microseconds) are possible today and several custom-build deposition systems have been successfully operated *in-situ* with GISAXS and GIWAXS at synchrotron facilities [15]. Along with this, laboratory-compatible tabletop X-ray sources also evolved over time. Complicated experiments that in the past could only be conducted at synchrotron facilities can now be performed in laboratories with some limitations.

4 Experimental Section

4.1 In-situ GISAXS tracking of 3D Ge QDs structure

In this experiment, a Ge/Al_2O_3 periodic multilayer containing 20 bilayers was deposited, starting with an Al_2O_3 layer on a Si(001) wafer with native oxide. Experiments were performed on a custom-designed dual ion beam sputtering (DIBS) apparatus (Bestec) with the *in-situ* GISAXS monitoring arrangement. The energy of Ar+ ion beam was set to 600 eV for our deposition. The sputtering targets Al_2O_3 and Ge with 99.9% purity were used (not in co-deposition mode). The average deposition rate of the target material was found to be 0.57 nm.min^{-1} and 2.7 nm.min^{-1} for Al_2O_3 and Ge targets, respectively. Following a previous study by *Buljan et al*., [16], the minimal layer thicknesses were fixed at 3 nm for Al_2O_3 and 1 nm for Ge. Henceforth, the deposition of one Al_2O_3 and one Ge layer took 315 s and 22 s, respectively. The period of multilayers and Γ value (Ge absorber thickness-to-period ratio) were kept constant at 4 nm and 0.25, respectively. After fixing the deposition rates, the final samples were prepared with 20 bilayers. The base pressure of 2×10^{-8} mbar dropped to 4×10^{-4} mbar during the deposition. The Ar gas flow into the ion guns was fixed to 5 sccm. Before the deposition, the samples were annealed at 523 K to remove surface contaminants. The depositions performed at 573 K and at room temperature (RT, 303 K) were compared.

The X-ray beam with a divergence of 1 mrad was produced by a 30 W microfocus X-ray source (IµS, Incoatec) assembled with semi-focusing Montel optics. X-ray photons with an energy of 8.04 keV (wavelength of 1.54 Å) were used. The primary X-ray beam coming out of the source with a flux of 1×10^8 photon s^{-1} (after the pinhole) hit the sample surface at a grazing incidence angle of 0.3°. This was above the critical angle of Ge for Cu Kα radiation, enabling the X-rays to penetrate the entire multilayer. The scattered X-ray intensity was monitored by a 2D hybrid X-ray detector (Pilatus 200K, Dectris). The scattered intensity was repetitively integrated for 5 s in a constant loop during the entire deposition. Henceforth, the series of GISAXS patterns taken frame after frame created a movie of the deposition process in reciprocal space. Furthermore, post-deposition *ex-situ* analyses such as TEM (JEOL 2100 F), GISAXS (Nanostar, Bruker AXS) and XRR (D8 Discover SSS, Bruker AXS) were performed.

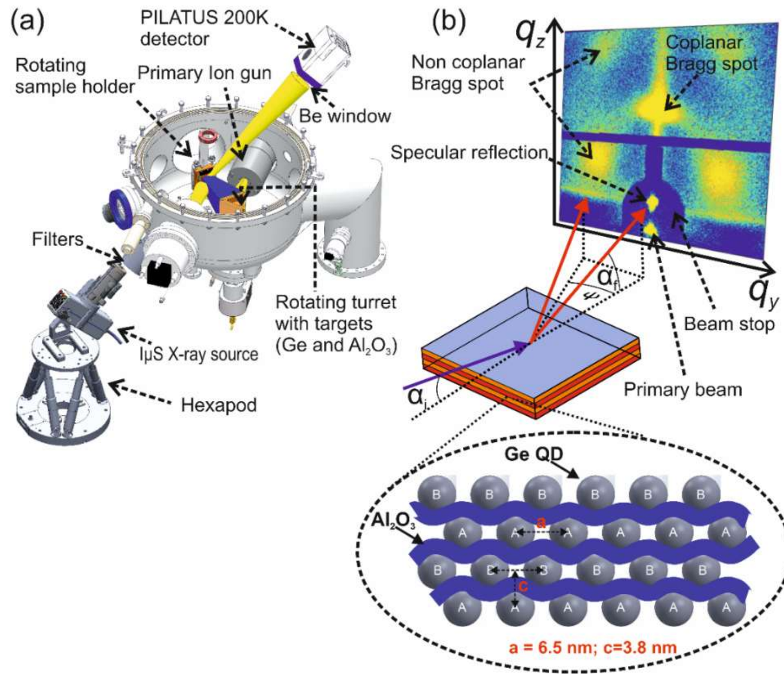

Figure 4.1 A sketch of the *in-situ* GISAXS experiment. (a) DIBS system fortified with a GISAXS setup. (b) Graphical representation of the GISAXS measurement geometry. The inset displays a periodic ABA stacking that is displayed by distinct Bragg spots on a 2D detector [17].

4.2 In-situ GIWAXS study of few-layer MoS_2

In this experiment few-layer MoS_2 films were fabricated on *c*-plane sapphire substrates by sulfurization of Mo layers with a thickness of 3 nm. The dimensions of the sapphire substrates used were 1×1 cm^2. The Mo layers were deposited by DC magnetron sputtering prior to the sulfurization process and details can be found in [18]. The few-layer MoS_2 films were prepared by a one-zone sulfurization process. The reactor is designed and built for *in-situ* GIWAXS monitoring of the deposition process at the synchrotron and in the laboratory (Figure 4.2). The amount of sulfur powder used in the experiment was 0.5 g, was heated under the sample, placed near the center of the CVD reactor. Mo layer was annealed in sulfur vapors at a temperature of 600°C in N_2 atmosphere at an ambient pressure for 30 minutes.

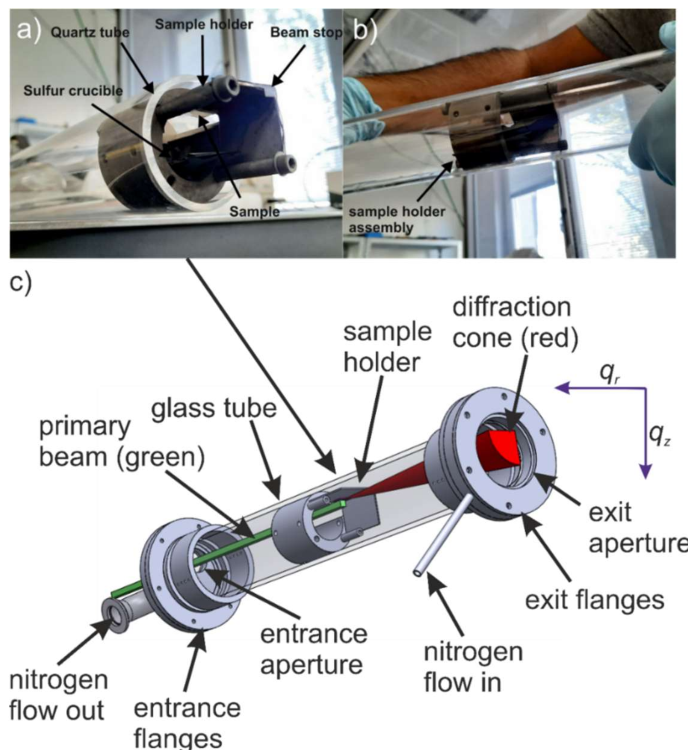

Figure 4.2 Photos of a) sample holder, b) loaded in CVD quartz tube and c) graphical illustration of the core of a CVD reactor.

Since the main objective of the experiment is to perform *in-situ* GIWAXS in a CVD reactor, standard CVD reactors are not suitable. So, the entire CVD reactor core was redesigned as per the experiment requirements. The sample is mounted in an inverted position inside of the sample holder for the better impinging of X-rays on its surface. The sample holder is also equipped with a slit (2.5 mm (H)×3 mm (V)) and a beam stop (3 mm×2 mm dimension) made from a thick Mo sheet (1mm thick).

***In-situ* GIWAXS measurements in synchrotron:**

The initial i*n-situ* GIWAXS measurements were executed at the SAXS beamline of the Elettra synchrotron radiation facility situated in Trieste, Italy. The energy of the X-ray photons used was 16 keV (wavelength of 0.7749 Å). The photon flux on the sample was around 10^{12} photons/s. The X-ray beam size was adjusted to 3 mm × 1 mm (H × V) by a slit system. The X-ray beam divergence was 0.3 mrad × 0.6 mrad (V × H). The entire CVD system was mounted on a heavy-duty hexapod (H-840, PI) which has six-axis of freedom. This allowed us to adjust tilt of the sample to the X-ray beam and set an angle of incidence of 0.2 deg.

The aluminum foils with a thickness of 30 µm each, having X-ray transparency of 95% at 16 keV photon energy was used in the entry and exit windows. The exit and entrance windows had a diameter of 55 mm and 20 mm, respectively. The non-reactive atmosphere inside of the CVD tube was maintained by nitrogen flow at a rate of 50 sccm and a pressure of 0.5 bar for HA MoS_2 and no flow for VA MoS_2. The distance between the sample and detector was fixed to 845 mm. The X-ray detector used in the experiment was a Pilatus3 1M (Dectris, Switzerland), a CMOS-based detector. The scattered X-ray intensity was captured continuously with an exposure time of 5 s and 10 s for the growth of VA $MoS_2$and HA MoS_2, respectively. During the *in-situ* experiment, organized sample displacement was observed due to thermal expansion of the sample holder assembly. It was compensated by counter-movements of the entire CVD chamber using the hexapod.

***In-situ* GIWAXS measurements in the laboratory:**

Real-time GIWAXS study of few-layer MoS_2 film fabricated from the sulfurization of MoO_3, were performed in the laboratory with the help of a 2nd generation high brilliance laboratory-based Mo X-ray source. Like before, the MoO_3 was deposited on *c*-plane sapphire substrates with a thickness of 10 nm. The Mo layers were deposited by DC magnetron and the samples were post annealed in the oxygen atmosphere (30 min in a 100 sccm O_2 flow at 450°C). The one-zone sulfurization process was carried out in the same custom-designed CVD reactor in He atmosphere (flow rate - 50 sccm and pressure – 0.5bar). The system was annealed from room temperature of 27°C to 600°C and maintained at 600°C for 1 hour (60 min). The temperature ramp was set to 4°C / min. The X-ray beam with a divergence of 4.9 mrad was produced by a 50 W microfocus high brilliance Mo-based X-ray source (IµS$^{\text{High Brilliance}}$ Mo, Incoatec) equipped with focusing Montel optics. X-ray photons with an energy of 17.45 keV (wavelength of 0.709 Å) were used.

A low-scatter pinhole of 1.3 mm diameter made of a Pt (250 µm) was used to calibrate the beam size and also to remove the unwanted diffuse X-ray scattering originating from the Montel optics and also from the Be exit window. The primary X-ray beam coming out of the source with a flux of 3.96×10^7 photon s^{-1} (after the pinhole) hit the sample surface at a grazing incidence angle of 0.3°. Here the X-ray source was mounted on a heavy-duty hexapod (H-840, PI) instead of the CVD chamber. The scattered X-ray intensity was continuously monitored by a 2D hybrid CMOS-based X-ray detector (Pilatus 200K, Dectris). The scattered intensity was repetitively integrated for 60 s in a constant loop during the entire deposition. Henceforth, the

evolution of the MoS_2 were tracked in real time with a series of GIWAXS patterns taken frame after frame till the end of the deposition process. Since the work is still in progress, only the preliminary results from *in-situ* studies were briefly presented at the end of this thesis.

Figure 4.3 Photo of the *in-situ* GIWAXS measurement setup in the laboratory.

5 Results and Discussion

5.1 *In-situ GISAXS tracking of 3D Ge QDs structure*

5.1.1 Temporal analysis layer by layer

The GISAXS pattern was taken constantly during the deposition process, with a 5 s time integration selected as a trade-off between the GISAXS intensity and temporal resolution. The selected GISAXS patterns taken at different stages of deposition are shown in Figure 5.1. Due to the temporal evaluation, bilayer by bilayer, the GISAXS frames given in Figure 5.1, were first spatially binned over 8 × 8 pixels of the detector. It is then integrated over one Ge/Al_2O_3 bilayer deposition time into one single frame. The insets in the figure show the simulated GISAXS maps.

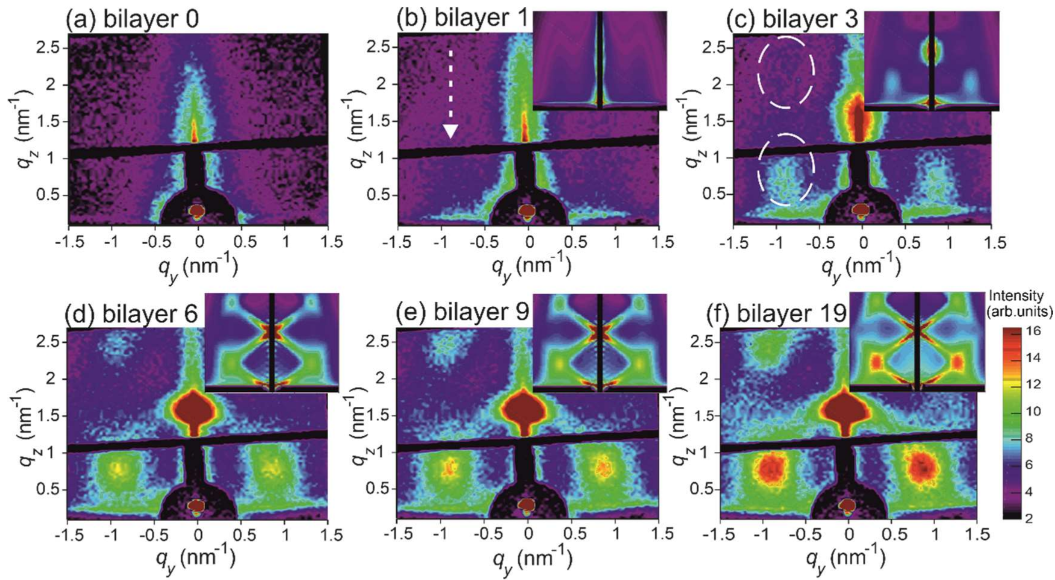

Figure 5.1 Selected Ge/Al_2O_3 multilayer GISAXS patterns grown at 573 K taken *in-situ* at various growth phases. Their corresponding mathematical simulations (insets) and the respective number of deposited bilayers are indicated (top left) [17].

In order to assess the temporal evolution of the lateral and vertical correlations of Ge QDs during the deposition of multilayer at 573 K layer by layer, we chose suitable regions of interest in the available GISAXS patterns. Here the intensity was integrated either along the q_y axis to show the intensity line profile along the q_z axis (for vertical) or vice versa. Figure 5.2 (a) and Figure 5.3 (a) display the last GISAXS patterns after the deposition of 20 bilayers, with the

selected regions of interest. It is indicated by the black dashed boxes. The integrated line profiles as a function of time and the number of bilayers for the evaluation of vertical and also horizontal QD correlations are shown in Figure 5.2 (b) and Figure 5.2 (c) and in Figure 5.3 (b) and Figure 5.3 (c), respectively.

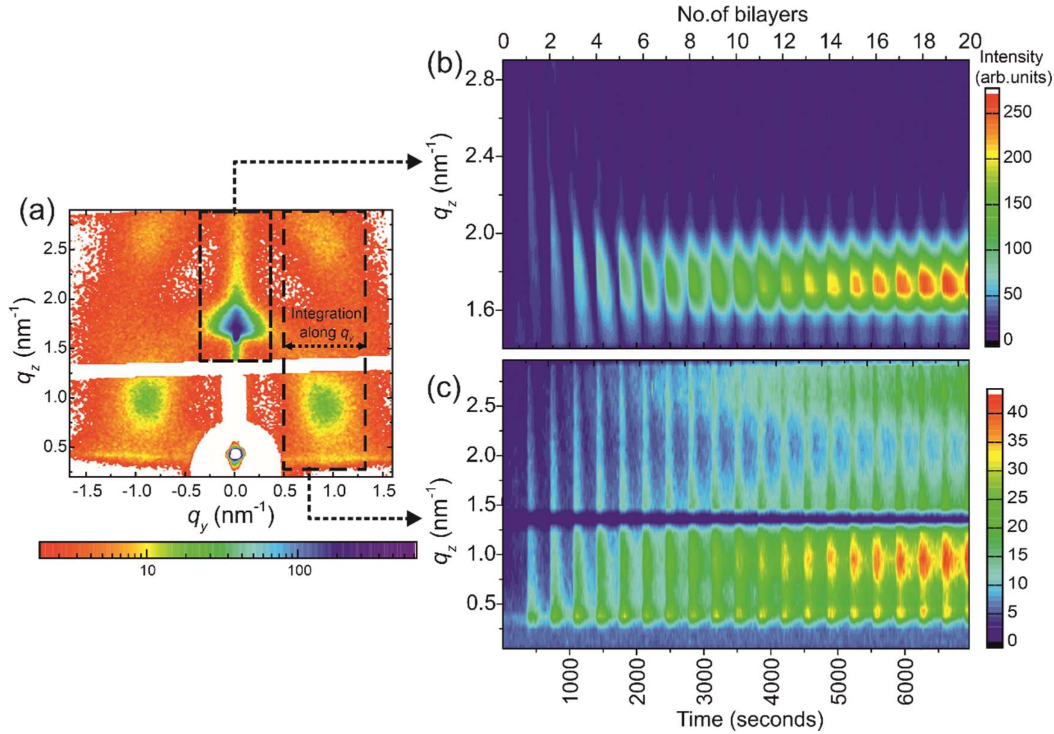

Figure 5.2 (a) The ultimate GISAXS pattern of the Ge/Al_2O_3 multilayer produced at 573 K with two selected regions of interest, indicated by the black dashed boxes. The intensity line profile from the temporal evolution along the q_z axis integrated between (b) $q_y = -0.48$ and 0.41 nm^{-1} and (c) $q_y = 0.40$ and 1.60 nm^{-1}. The unfilled region is the shadow of beamstop and a stitch between two modules (dead area) of the 2D detector [17].

Figure 5.2 shows that the vertical correlation of Ge QDs is preserved during the whole multilayer deposition process. The ABA stacking of Ge QDs is reinforced by theoretical simulations of the intensity distribution in reciprocal space, based on a 3D paracrystal model.

The temporal evolution of the GISAXS line profiles along the q_y axis delivers information about the Ge QD ordering in the lateral (sideways) direction (along the substrate). It suggests the existence of a uniaxial anisotropy of QD-ordered domains with the surface normal being the principal axis. Because of the same phenomenon, the temporal evolutions of the two profiles are alike. The symmetrical peaks originate after the first Ge layer deposition and raise

in intensity during the successive deposition cycles. This suggests that the first QD layer act as a seed template. It defines the in-plane (lateral) inter-QD separation (distances) across the entire 3D Ge QD structure.

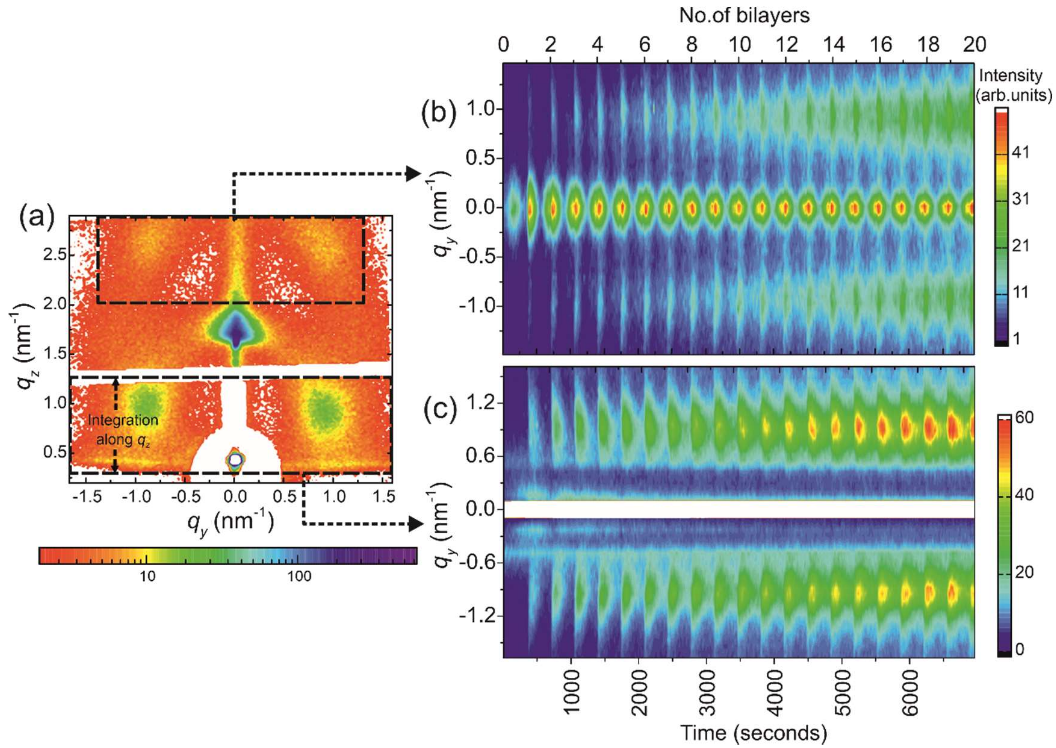

Figure 5.3 (a) The ultimate GISAXS pattern of the Ge/Al_2O_3 multilayer grown at 573 K with two selected regions of interest. It is indicated by the dashed black boxes. The time-based evolution of the intensity line profile along the q_y axis is integrated between (b) q_z = 1.93 and 2.97 nm^{-1} and (c) q_z = 0.20 and 1.24 nm^{-1} [17].

Additionally, we performed a post-deposition *ex-situ* measurement of the deposited samples on a dedicated laboratory GISAXS system having a larger q_z range. Due to the higher primary beam flux of the Excillum X-ray source and the larger collection time, the *ex-situ* GISAXS pattern also shows the second- and even third-order Bragg peaks at q_y = 0.0 nm^{-1}, as shown in Figure 5.6 (b). The first and second-order side maxima are also clearly observable in Figure 5.6 (b) and backing the ABA stacking of Ge QDs. Additionally, weak third- and fourth-order side maxima are visible, in which the former being partially blocked by the dead area between two modules of the 2D detector.

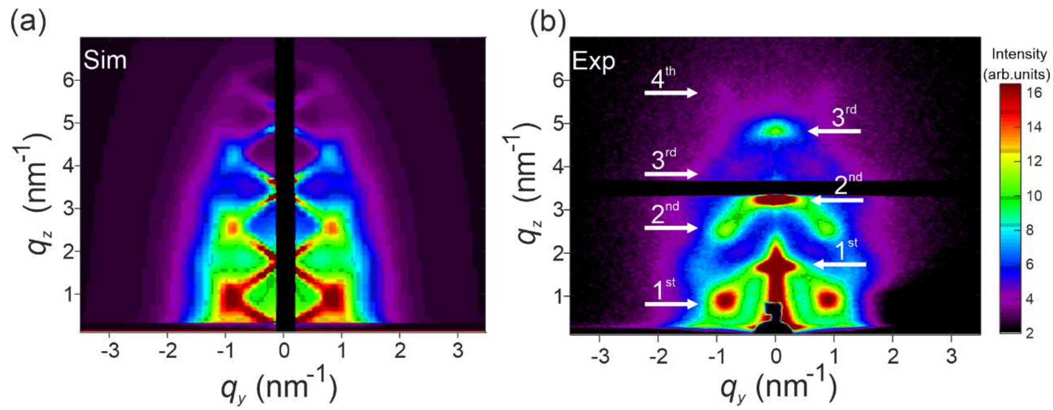

Figure 5.6 The (a) simulated and (b) *ex-situ* measured GISAXS patterns of the Ge/Al_2O_3 multilayer deposited at 573 K, in a larger q_z range. The first three orders of Bragg peaks are specified by the white arrows on the right. The first four orders of the side maxima are specified by the white arrows on the left [17].

The simulation of the experimental GISAXS pattern is given in Figure 5.6 (a). For the simulation, the paracrystal model suggested by Buljan et al. [16] was implemented. To study the arrangement and shape of Ge QDs in real space, HR-TEM of the Ge/Al_2O_3 multilayer was employed. Figure 5.8 shows the cross-section HR-TEM image of the sample grown at 573 K.

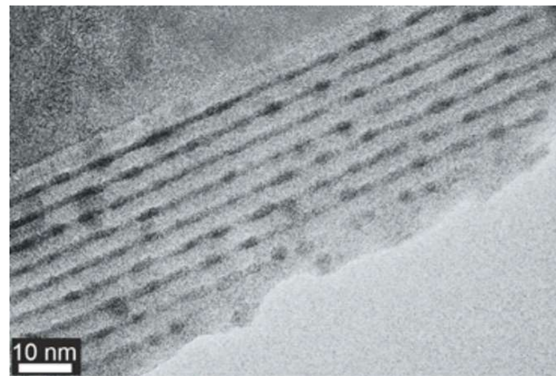

Figure 5.8 A cross-section HR-TEM image of Ge QDs embedded in the Al_2O_3 matrix after the multilayer deposition at 537 K [17].

5.2 *In-situ GIWAXS study of few-layer MoS_2 films*

5.2.1 *In-situ* Synchrotron GIWAXS measurements

The GIWAXS patterns collected before and after sulfurization of Mo films at a nitrogen flow rate of 50 sccm are given in Figure 5.10 (a) and Figure 5.10 (b), respectively. After sulfurization, the layer shows a strong 002 diffraction spot positioned along the q_z direction at q_z = 1 $Å^{-1}$. This indicates that the (001) lattice planes of MoS_2 are positioned parallel to the sample surface with the *c*-axis oriented along the substrate surface normal, equivalent to HA MoS_2 films.

Alternatively, GIWAXS patterns collected before and after sulfurization of Mo films at zero flow rate of nitrogen are shown in Figure 5.10 (c) and Figure 5.10 (d), respectively. The 002 diffraction spot oriented along the q_r direction at q_r = 1 $Å^{-1}$ confirms the presence of a perpendicular orientation of the (001) lattice planes with respect to the sample surface with the *c*-axis aligned in the plane of the film. This corresponds to VA MoS_2 films. We observed that the elastic X-ray scattering of the primary beam in N_2 atmosphere of the CVD chamber is responsible for the strong observed intensity pattern close to the origin of reciprocal space in all GIWAXS maps. Additionally, the unreachable region of GIWAXS pattern along the q_z direction at q_r = 0 $Å^{-1}$, also known as the "*missing wedge*", which is characteristic to the scattering geometry used, prevents a direct evaluation of the total phase volumes in HA and VA MoS_2 films [19].

The CVD heating ramp of 25°C/min and the maximum temperature of 600°C kept for 30 minutes were common for both orientations of MoS_2. In the HA MoS_2 sample, the inert atmosphere inside the CVD reactor was preserved with a nitrogen flow rate of 50 sccm. This decreased the sulfur partial vapor pressure on the sample. In contrast, for VA MoS_2, no nitrogen flow through the CVD chamber was used. In its place, it was only purged with nitrogen prior to the heating process. Chance of gas backflow was prohibited by using a one-way valve at the outlet of the CVD chamber. Thus, the sulfur partial vapor pressure on the sample was higher throughout the growth of VA MoS_2 than during the growth of HA MoS_2.

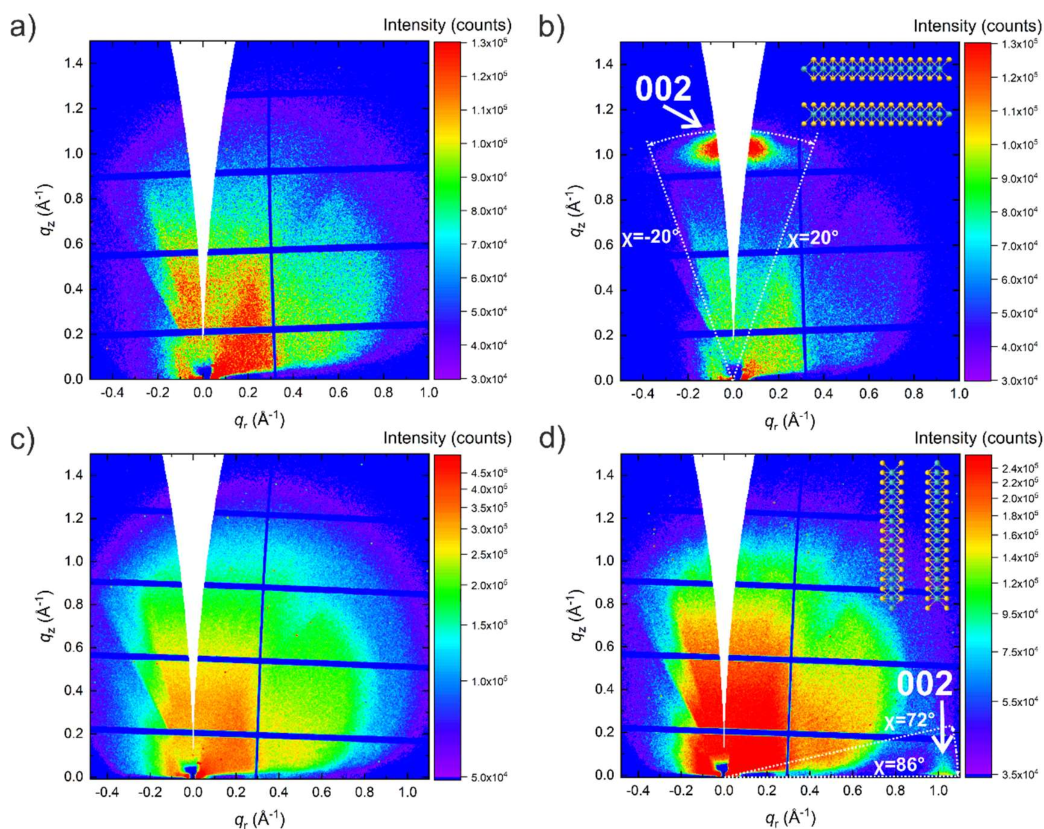

Figure 5.10 Sulfurization of Mo films at two different N_2 flows rates. GIWAXS patterns of a) early Mo and b) last HA MoS_2 film after sulfurization at a flow rate of 50 sccm and c) initial Mo and d) final VA MoS_2 film after sulfurization at zero rate of flow. The insets represent the orientation of MoS_2 layers. The dashed lines specify the limits for the profile integration.

The selected intensity profiles of the 002 diffraction peak taken along the q_z direction within the χ range (-20°, +20°), during the phase transformation process leading to HA MoS_2 are given in Figure 5.12 (a). For the purpose comparison, intensity profiles taken out along the q_r (which is in-plane) direction with the χ range (72°, 86°) are shown in Figure 5.12 (b). It was used to follow the Mo phase transformation towards VA MoS_2. In both scenarios, the beginning of the early phase transformation towards the MoS_2 phase can be already seen close to 450°C. The analysis of the phase diagram of the Mo-S system in the sulfur-rich area (S/Mo > 2) under a pressure of 1 atmosphere exposes a universal CVD growth window for the MoS_2 phase from sulfur gas, starting at 444.6°C. This coincides well with the beginning of the phase transition

observed in our experiment. The phase transition attains saturation for temperatures above 500°C. The gradual narrowing of the 002 diffraction peak specifies an increase in the size of coherently scattering domains of MoS_2 crystals in both HA and VA films. An important observation in our experiments is the growth evolution is either exclusively VA or exclusively HA MoS_2 phases. No reorientations between the two were noticed during the sulfurization process. This proposes that the extent of the sulfur diffusion decides the final orientation from the vapor-solid interface into the bulk. Furthermore, it is evident that once the growth of a given orientation has nucleated, there is no possibility of switching back.

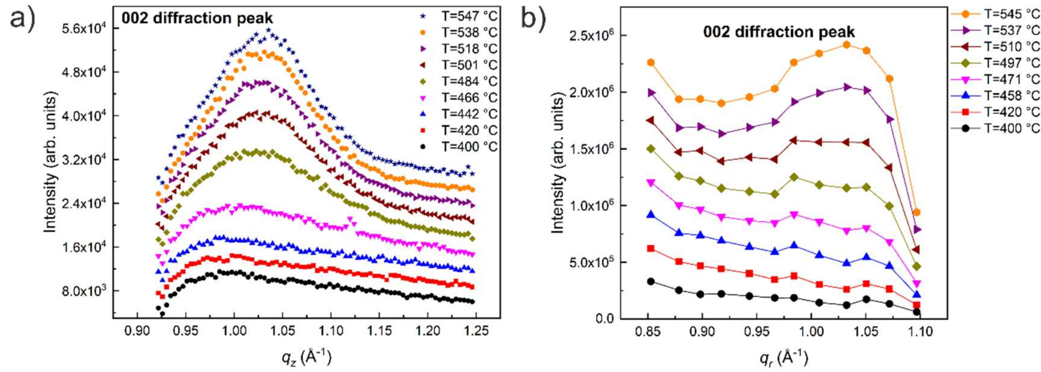

Figure 5.12 The 002 intensity (cuts) profiles for a) HA MoS_2 and b) VA MoS_2 films at different deposition temperatures.

To deliver a quantitative analysis of phase transformations for both HA and VA orientations, the normalized integral intensities of the 002 diffraction peaks for HA and VA MoS_2 are plotted as functions of time and temperature in Figure 5.13 (a). Both VA and HA aligned MoS_2 samples display a similar evolution of the area under the 002 diffraction peak. To simplify the understanding of the phase transformations in both cases and to quantify the analysis, we applied the mathematical models developed by Avrami and Dietz [20–22]. The activation energy was estimated by applying the Avrami model, because it delivers the most accurate crystallization kinetics model.

In the mathematical modeling, the temperature was assumed to be linear with time. The Avrami model delivered activation energies of 329±3 $kJ.mol^{-1}$ and 324±2 $kJ.mol^{-1}$ for VA and HA MoS_2, respectively. The published values of activation energies [23,24] for sulfurization of bulk Mo films were in the range of 105 $kJ.mol^{-1}$ to 326 $kJ.mol^{-1}$. Depended on the measured values of activation energies for both orientations, it can be determined that the growth of differently oriented MoS_2 has comparable activation energies within their corresponding

confidence intervals. Since the only dissimilar growth parameter was the nitrogen gas flow, the beginning of the different orientation should therefore be seen in the different sulfur vapor pressure.

Furthermore, due to the improved statistics of the scattered X-ray data for the growth of HA MoS_2 and similarities in the activation energies with VA MoS_2, we have executed the refined fitting technique only for HA MoS_2 films. The Avrami model was effective in describing the initial stage of kinetics of transformation. However, it fails to define the slowdown of the crystallization process at the temperatures above the phase transition in the range between 500°C and 550°C, which is also known as the post-Avrami or secondary crystallization [21,25]. To recover from this drawback of the Avrami model, a modified Avrami model, known as Dietz model, was applied [26]. The blue line represents the best fit result of the Dietz model for HA MoS_2 in Figure 5.13 (a). Even though, as it can be seen, the implementation of the modified Avrami model does not change the activation energies and only influences the secondary crystallization rate as predicted.

Lastly, to evaluate the change in film mosaicity $\Delta\chi$ during the film sulfurization process, which is the average misalignment of the crystal *c*-axis in reference to the surface normal, we performed χ-cuts from the GIWAXS patterns. For the growth of HA MoS_2, FWHM of the χ-cuts integrated in the q range 0.95 – 1.10 $Å^{-1}$ are depicted in Figure 5.13 (c). We detect a decreasing angular misalignment $\Delta\chi$ of MoS_2 crystals from the substrate surface's normal direction during the primary phase of nucleation and crystal growth.

Based on the investigation results, the observed difference in the growth of HA versus VA MoS_2 depends exclusively on the concentration of S atoms at the vapor-solid interface because all other deposition or reaction parameters were kept constant. The growth of either VA or HA MoS_2 is controlled by an equilibrium between the surface energy of the final film and the reactivity of Mo with S. The result from this study put forward the fact that the growth of VA MoS_2 at high S concentration is preferable over HA due to the efficient and rapid growth of MoS_2 phase. In that case, the fast diffusion kinetics of S into Mo bulk due to high sulfur pressure, forming MoS_2 phase, even succeeded over the lower surface energy offered by the alternative HA configuration. On the other hand, under S deficient conditions made by N_2 flow, the lower surface energy of the HA configuration overshadows the rapid diffusion-controlled growth of the VA configuration

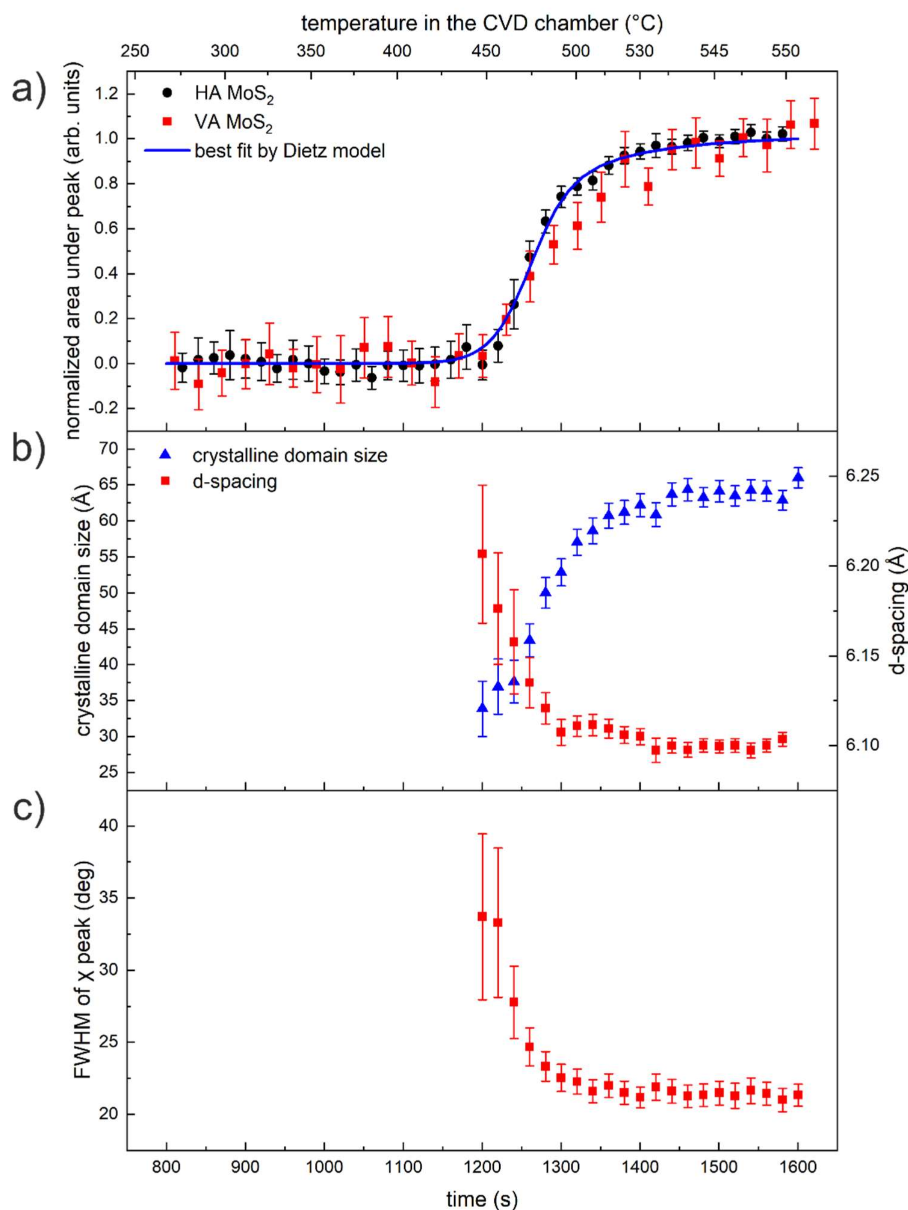

Figure 5.13 a) The normalized 002 diffraction intensity profile for VA and HA MoS_2 layers as a function of time and temperature. The blue line in the graph renders the best fit by the Dietz model for the growth of HA MoS_2. b) Calculated coherent crystalline domain size along with d-spacing. c) FWHM of χ profile (intensity cuts) as a function of time and temperature.

5.2.2 Laboratory based *in-situ* GIWAXS measurements

The real-time *in-situ* GIWAXS study of sulfurization of few-layer MoO_3 to obtain MoS_2 layers was carried out in the laboratory with the help of high brilliance Mo X-ray microfocus

source. The experiments were performed in the same custom-designed CVD chamber. Figure 4.3 shows the images of the assembled experimental setup in the laboratory. The GIWAXS patterns obtained from the initial set of experiments performed in the laboratory confirm the presence of MoO_2 during the sulfurization process, shown in Figure 5.15 to Figure 5.17. As for now, it was only proven by various *ex-situ* measurements that the MoO_3 reduces to MoO_2 during the sulfurization as per the chemical reaction in theory [27]. The GIWAXS patterns taken before, in the middle and after sulfurization of MoO_3 film at a He flow rate of 50 sccm are shown in Figure 5.15, Figure 5.16 and Figure 5.17, respectively. Before sulfurization, the MoO_3 layer shows a strong 200 diffraction spot located along the q_r direction at $q_r = 0.9$ Å^{-1} for a $\chi = 60°$. When the temperature of the CVD reactor reaches around 527°C the MoO_2 diffraction peak starts to appear along with MoO_3 diffraction, at $q_r = 1.8$ Å^{-1} for a $\chi = 45°$ (Figure 5.15).

Around 567°C, the MoO_3 totally disappears and a stronger MoO_2 diffraction alone appears (Figure 5.16). When the system's temperature reaches its peak, at 600°C the MoS_2 peak originates at $q_z = 1$ Å^{-1}. The coexistence of the MoS_2 peak along with the MoO_2 diffraction peak substantiate the intermittent stage of MoO_2 in the sulfurization process of MoS_2 from MoO_3, as in the chemical reaction formula [27], shown in Figure 5.17 (a and c). At the end of the rection process, a strong 002 diffraction spot located along the q_z direction at $q_z = 1$ Å^{-1} corresponding to MoS_2 film emerged, which is shown in Figure 5.17 (b and d).

The additional diffraction ring above the MoS_2 is from the Ta beam stop used in the experiment. Since the main experiment is still in progress, we are unable to present further results in the current section. The results presented are from the preliminary data obtained in the laboratory.

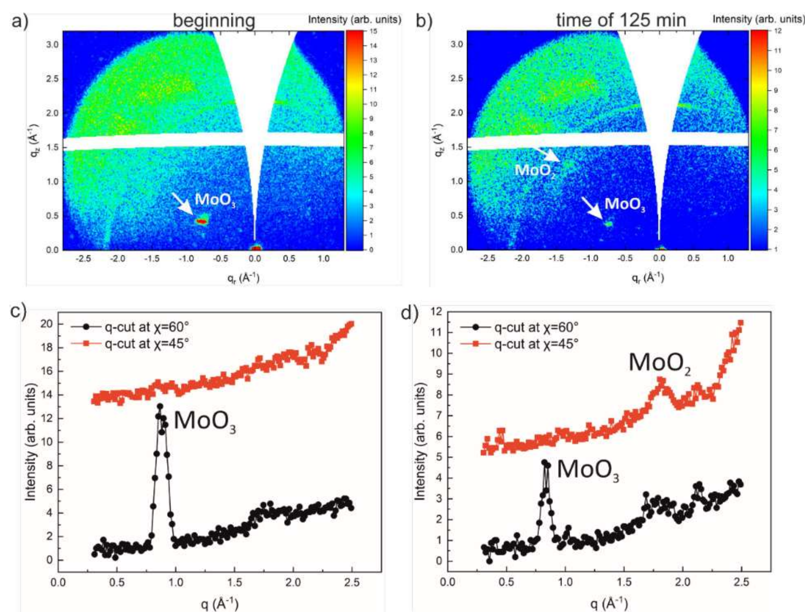

Figure 5.15 *In-situ* GIWAXS patterns taken at a) at the beginning, b) at 125th minute of the heating process. c) and d) Extracted intensity profiles from the GIWAXS patterns in χ range between 45° and 60°.

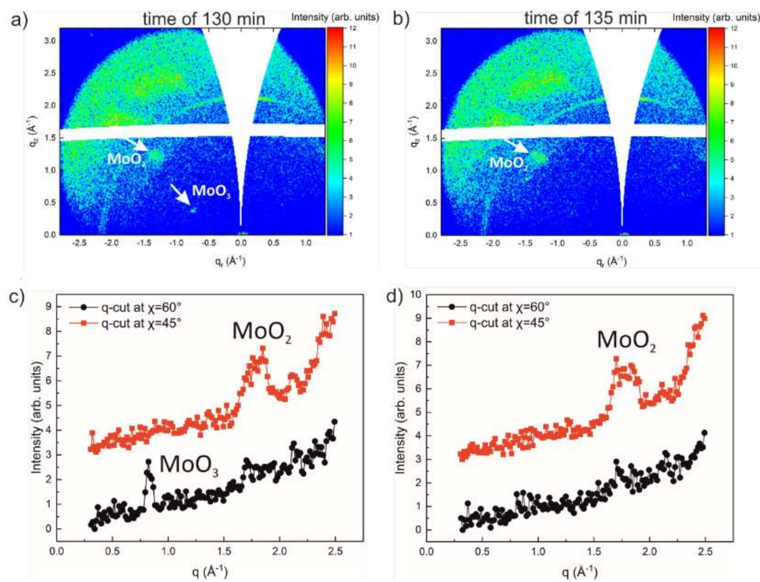

Figure 5.16 *In-situ* GIWAXS patterns taken at a) at 130th minute, b) at 135th minute of the heating process, c) and d) Extracted intensity profiles from the GIWAXS patterns

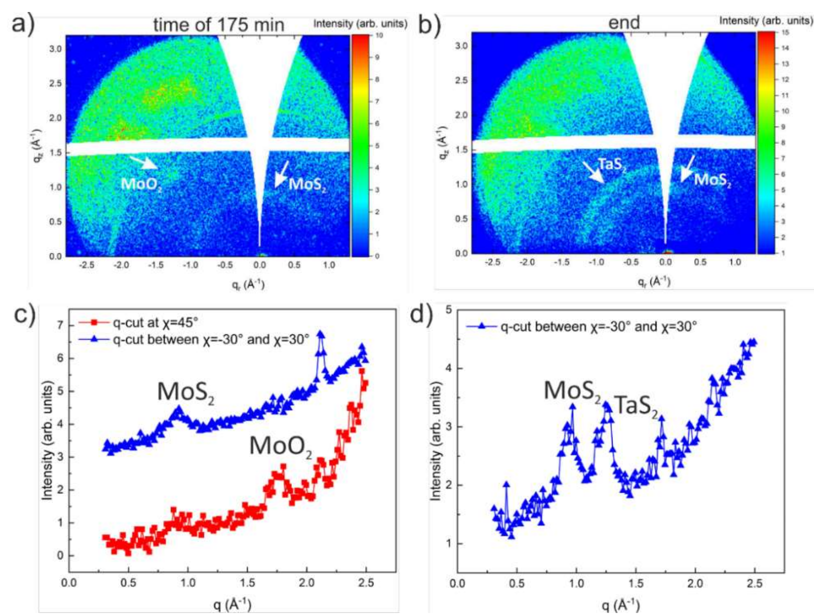

Figure 5.17 *In-situ* GIWAXS patterns taken at a) at 175th minute, b) at the end of the heating process, c) and d) Extracted intensity profiles from the GIWAXS patterns in χ range between 45° and 60°.

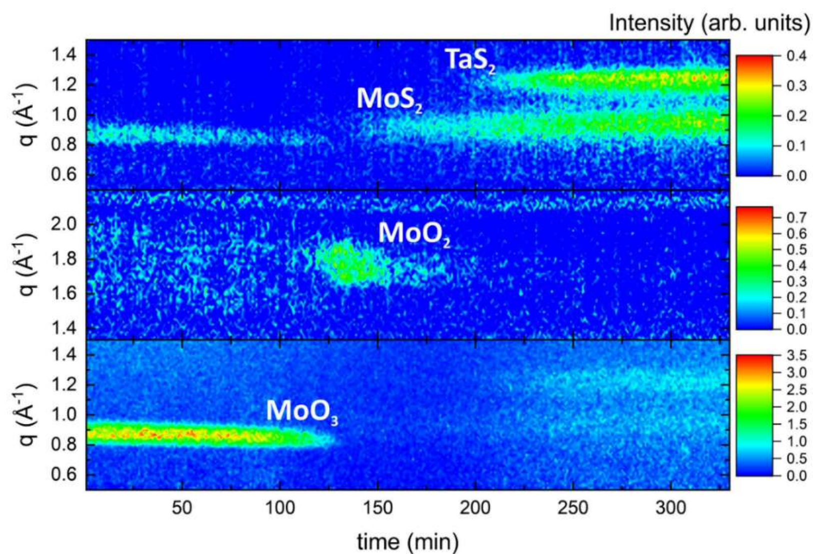

Figure 5.18 Temporal evolution of the MoO_3 peak to MoS_2 in reciprocal space as a function of deposition time.

The temporal evolution of the MoS_2 from MoO_3 through MoO_2 as a function of time is shown in Figure 5.18. The data are shown as a function of time since the calibration of data as a function of temperature on the substrate is still under progress. Finally, experiments like this prove the potential and possibilities of the laboratory *in-situ* X-ray scattering experiments,

which opens new doors to the *in-situ* and real-time GIWAXS studies of 2D TMD materials in a laboratory facility.

6 Conclusion

. The primary goal of my PhD thesis was to perform the study of thin film growth on 2D materials by *in-situ* X-ray scattering. This goal was successfully fulfilled by implementing and developing a custom-designed GISAXS/GIWAXS setup. The first achievement is related to implementing a dual ion beam sputtering deposition system equipped with a microfocus X-ray source and 2D X-ray detector by performing in laboratory *in-situ* GISAXS study. This helps us to tackle the 3D QD structural evolution in multilayers. The second significant achievement is the devolvement of a custom-designed CVD reactor suitable for *in-situ* GIWAXS experiments. The goal to design a system compatible with both synchrotron and laboratories was successfully achieved. In addition, the aim to transfer GIWAXS technique on the 2D TMD materials from synchrotrons to the laboratories was also successfully attained. Both of the systems are unique and tailored specially for our purposes. The devices are currently installed at the Department of multilayers and nanostructures, Institute of Physics, Slovak Academy of Sciences, Bratislava.

In this work, we studied the self-assembly method resulting in the formation of a 3D Ge QD structure in an amorphous Al_2O_3 matrix in real time during the deposition of a periodic Ge/Al_2O_3 multilayer at substrate temperatures 303K and 573 K. The higher temperature of substrate proved to be essential to achieve the self-assembly effect. The temporal GISAXS resolution permitted us to track the self-aligning growth mechanism of Ge QDs layer after layer. It was further confirmed by *the ex-situ* TEM and XRR studies. The spots of interference originating in the vertical and lateral ordering of the Ge QDs representing a body-centered tetragonal structure with ABA Ge QD assembling emerged in the *in situ* GISAXS patterns after deposition of three Ge/ Al_2O_3 bilayers. The last GISAXS pattern analyzed *ex-situ* over a larger **q** range and fitted within a 3D paracrystal model confirmed the ABA stacking of QDs and delivered the main structural parameters of the 3D Ge QD structure with reference to the lattice parameters and their deviations. A simulation of temporal evolution of the FWHM corresponding to first-order side maximum based on this paracrystal model displayed perfect agreement with the experimental values coming from the bilayer-by-bilayer investigation of

the *in-situ* GISAXS patterns. The attained results are significant for the application of materials created on regularly ordered Ge QDs implanted in alumina.

Control over the crystalline orientation of few-layer MoS_2 films plays an essential role in determining its applications. We executed a controlled sulfurization process of Mo-coated substrates in a one-zone CVD reactor by keeping all deposition parameters constant, except the nitrogen flow through the reactor. We proved that in the case of rapid sulfurization, the partial sulfur vapor pressure is the critical factor that controls the orientation of the final few-layer MoS_2 films. VA and HA MoS_2 films were fabricated without and with flow of nitrogen. The activation energies of Mo sulfurization important to HA or VA MoS_2 appear to be basically identical, as proved by *in-situ* GIWAXS. The beginning of the different MoS_2 orientations at different sulfur vapor pressures can be described by the balance between the fast sulfur diffusion along the vdW gap and surface energy minimization that leads to VA or HA MoS_2. Even though the results presented are promising, it still leaves areas that need a deeper understanding of the delicate balance between the growth of HA and VA $MoS_{2.}$

In section 5.2.2, we followed real-time kinetics of the sulfurization process of MoO_3 by *in-situ* GIWAXS in a laboratory setup. The initial set of results presented confirm the existence of MoO_2 during the fabrication of MoS_2 via sulfurization of trioxide. The presented real-time GIWAXS results open the possibility to study the physical and chemical phenomena behind the phase transformations in a large number of low-dimensional TMD materials in CVD reactors in general. Further experimental and theoretical studies are necessary to understand the mechanisms behind the findings fully.

The results obtained from these experiments demonstrate the potential of real-time *in-situ* GISAXS/GIWAXS monitoring to provide efficient feedback for deposition. It also provides an understanding about the growth process and interface morphology, without the necessity of synchrotron sources that are usually overbooked and require long-term planning.

7 List of author's publications

[1] **A. Shaji**, K. Vegso, M. Sojkova, M. Hulman, P. Nadazdy, P. Hutar, L. Pribusova Slusna, J. Hrda, M. Bodik, M. Hodas, S. Bernstorff, M. Jergel, E. Majkova, F. Schreiber, P. Siffalovic, Orientation of Few-Layer MoS_2 Films: In-Situ X-ray Scattering Study During Sulfurization, J. Phys. Chem. C. (2021) acs.jpcc.1c01716. https://doi.org/10.1021/acs.jpcc.1c01716.

[2] **A. Shaji**, M. Micetic, Y. Halahovets, P. Nadazdy, I. Matko, M. Jergel, E. Majkova, P. Siffalovic, Real-time tracking of the self-assembled growth of a 3D Ge quantum dot lattice in an alumina matrix, J. Appl. Crystallogr. 53 (2020) 1029–1038. https://doi.org/10.1107/S1600576720007815.

[3] M. Bodik, M. Demydenko, T. Shabelnyk, Y. Halahovets, M. Kotlar, D. Kostiuk, **A. Shaji**, A. Brunova, P. Veis, M. Jergel, E. Majkova, P. Siffalovic, Collapse Mechanism in Few-Layer MoS_2 Langmuir Films, J. Phys. Chem. C. 124 (2020) 15856–15861. https://doi.org/10.1021/acs.jpcc.0c02365.

[4] J. Hagara, N. Mrkyvkova, L. Feriancová, M. Putala, P. Nádaždy, M. Hodas, **A. Shaji**, V. Nádaždy, M.K. Huss-Hansen, M. Knaapila, J. Hagenlocher, N. Russegger, M. Zwadlo, L. Merten, M. Sojková, M. Hulman, A. Vlad, P. Pandit, S. Roth, M. Jergel, E. Majková, A. Hinderhofer, P. Siffalovic, F. Schreiber, Novel highly substituted thiophene-based n-type organic semiconductor: structural study, optical anisotropy and molecular control, CrystEngComm. 22 (2020) 7095–7103. https://doi.org/10.1039/D0CE01171A.

[5] P. Hutár, M. Sojková, I. Kundrata, K. Vegso, **A. Shaji**, P. Nádaždy, L. Pribusová Slušná, E. Majková, P. Siffalovic, M. Hulman, Correlation Between the Crystalline Phase of Molybdenum Oxide and Horizontal Alignment in Thin MoS_2 Films, J. Phys. Chem. C. 124 (2020) 19362–19367. https://doi.org/10.1021/acs.jpcc.0c05336.

[6] **A. Shaji**, J. James, P. Nancy, From nature: Optics, nanotechnology, and nano-optics, in: Nano-Optics, Elsevier, 2020: pp. 1–18. https://doi.org/10.1016/B978-0-12-818392-2.00001-9.

[7] P. Nancy, J.A. Mathew, J. Jose, J. James, B. Joseph, **A. Shaji**, S. Thomas, N. Kalarikkal, Laser, nanoparticles, and optics, in: Nano-Optics, Elsevier, 2020: pp. 47–65. https://doi.org/10.1016/B978-0-12-818392-2.00004-4.

[8] J. James, B. Chandra, B. Joseph, P. Nancy, **A. Shaji**, J. Jose, N. Kalarikkal, Y. Grohens, G. Vignaud, S. Thomas, Nano-optics: Challenges, trends, and future, in: Nano-Optics, Elsevier, 2020: pp. 19–32. https://doi.org/10.1016/B978-0-12-818392-2.000020.

[9] J. James, B. Joseph, **A. Shaji**, P. Nancy, N. Kalarikkal, S. Thomas, Y. Grohens, G. Vignaud, Microscopic Analysis of Plasma-Activated Polymeric Materials, in: Non-Thermal Plasma Technol. Polym. Mater., Elsevier, 2019: pp. 287–317. https://doi.org/10.1016/B978-0-12-813152-7.00011-1.

[10] **A. Shaji**, A.K. Zachariah, Surface Area Analysis of Nanomaterials, in: Therm. Rheol. Meas. Tech. Nanomater. Charact., Elsevier, 2017: pp. 197–231. https://doi.org/10.1016/B978-0-323-46139-9.00009-8.

[11] R.K. Mishra, **A. Shaji**, S. Thomas, Processing, rheology, barrier properties, and theoretical study of microfibrillar and nanofibrillar in situ composites, in: Micro Nano Fibrillar Compos. (MFCs NFCs) from Polym. Blends, Elsevier, 2017: pp. 233–262. https://doi.org/10.1016/B978-0-08-101991-7.00010-8.

8 Bibliography

[1] J.E. Greene, Tracing the 5000-year recorded history of inorganic thin films from ∼3000 BC to the early 1900s AD, Appl. Phys. Rev. 1 (2014) 041302. https://doi.org/10.1063/1.4902760.

[2] A. Lakhtakia, R. Messier, History of Thin-Film Morphology, in: Sculpt. Thin Film. Nanoeng. Morphol. Opt., SPIE, 1000 20th Street, Bellingham, WA 98227-0010 USA, 2009: pp. 27–48. https://doi.org/10.1117/3.585322.ch2.

[3] J. Shen, Z. Gai, J. Kirschner, Growth and magnetism of metallic thin films and multilayers by pulsed-laser deposition, Surf. Sci. Rep. 52 (2004) 163–218. https://doi.org/10.1016/j.surfrep.2003.10.001.

[4] V. Bressler-Hill, S. Varma, A. Lorke, B.Z. Nosho, P.M. Petroff, W.H. Weinberg, Island Scaling in Strained Heteroepitaxy: InAs/GaAs(001), Phys. Rev. Lett. 74 (1995) 3209–3212. https://doi.org/10.1103/PhysRevLett.74.3209.

[5] O. Crespo-Biel, B.J. Ravoo, D.N. Reinhoudt, J. Huskens, Noncovalent nanoarchitectures on surfaces: from 2D to 3D nanostructures, J. Mater. Chem. 16 (2006) 3997. https://doi.org/10.1039/b608858a.

[6] G. Renaud, Real-Time Monitoring of Growing Nanoparticles, Science (80-.). 300 (2003) 1416–1419. https://doi.org/10.1126/science.1082146.

[7] R. Lazzari, F. Leroy, G. Renaud, Grazing-incidence small-angle x-ray scattering from dense packing of islands on surfaces: Development of distorted wave Born approximation and correlation between particle sizes and spacing, Phys. Rev. B. 76 (2007) 125411. https://doi.org/10.1103/PhysRevB.76.125411.

[8] S. Manzeli, D. Ovchinnikov, D. Pasquier, O. V. Yazyev, A. Kis, 2D transition metal dichalcogenides, Nat. Rev. Mater. 2 (2017) 17033. https://doi.org/10.1038/natrevmats.2017.33.

[9] K.F. Mak, C. Lee, J. Hone, J. Shan, T.F. Heinz, Atomically thin MoS_2: A new direct-gap semiconductor, Phys. Rev. Lett. 105 (2010) 136805. https://doi.org/10.1103/PhysRevLett.105.136805.

[10] J. Hagara, N. Mrkyvkova, P. Nádaždy, M. Hodas, M. Bodík, M. Jergel, E. Majková, K.

Tokár, P. Hutár, M. Sojková, A. Chumakov, O. Konovalov, P. Pandit, S. Roth, A. Hinderhofer, M. Hulman, P. Siffalovic, F. Schreiber, Reorientation of π-conjugated molecules on few-layer MoS_2 films, Phys. Chem. Chem. Phys. 22 (2020) 3097–3104. https://doi.org/10.1039/C9CP05728E.

[11] J. Stangl, V. Holý, T. Roch, A. Daniel, G. Bauer, J. Zhu, K. Brunner, G. Abstreiter, Grazing incidence small-angle x-ray scattering study of buried and free-standing SiGe islands in a SiGe/Si superlattice, Phys. Rev. B. 62 (2000) 7229–7236. https://doi.org/10.1103/PhysRevB.62.7229.

[12] S.G. Podorov, N.N. Faleev, K.M. Pavlov, D.M. Paganin, S.A. Stepanov, E. Förster, A new approach to wide-angle dynamical X-ray diffraction by deformed crystals, J. Appl. Crystallogr. 39 (2006) 652–655. https://doi.org/10.1107/S0021889806025696.

[13] A. Hexemer, P. Müller-Buschbaum, Advanced grazing-incidence techniques for modern soft-matter materials analysis, IUCrJ. 2 (2015) 106–125. https://doi.org/10.1107/S2052252514024178.

[14] S. Kowarik, Thin film growth studies using time-resolved x-ray scattering, J. Phys. Condens. Matter. 29 (2017) 043003. https://doi.org/10.1088/1361-648X/29/4/043003.

[15] L.J. Richter, D.M. DeLongchamp, F.A. Bokel, S. Engmann, K.W. Chou, A. Amassian, E. Schaible, A. Hexemer, In Situ Morphology Studies of the Mechanism for Solution Additive Effects on the Formation of Bulk Heterojunction Films, Adv. Energy Mater. 5 (2015) 1400975. https://doi.org/10.1002/aenm.201400975.

[16] M. Buljan, N. Radić, S. Bernstorff, G. Dražić, I. Bogdanović-Radović, V. Holý, Grazing-incidence small-angle X-ray scattering: application to the study of quantum dot lattices, Acta Crystallogr. Sect. A Found. Crystallogr. 68 (2012) 124–138. https://doi.org/10.1107/S0108767311040104.

[17] A. Shaji, M. Micetic, Y. Halahovets, P. Nadazdy, I. Matko, M. Jergel, E. Majkova, P. Siffalovic, Real-time tracking of the self-assembled growth of a 3D Ge quantum dot lattice in an alumina matrix, J. Appl. Crystallogr. 53 (2020) 1029–1038. https://doi.org/10.1107/S1600576720007815.

[18] M. Sojková, K. Vegso, N. Mrkyvkova, J. Hagara, P. Hutár, A. Rosová, M. Čaplovičová, U. Ludacka, V. Skákalová, E. Majková, P. Siffalovic, M. Hulman, Tuning the

orientation of few-layer MoS_2 films using one-zone sulfurization, RSC Adv. 9 (2019) 29645–29651. https://doi.org/10.1039/C9RA06770A.

[19] J.L. Baker, L.H. Jimison, S. Mannsfeld, S. Volkman, S. Yin, V. Subramanian, A. Salleo, A.P. Alivisatos, M.F. Toney, Quantification of Thin Film Crystallographic Orientation Using X-ray Diffraction with an Area Detector, Langmuir. 26 (2010) 9146–9151. https://doi.org/10.1021/la904840q.

[20] M. Avrami, Granulation, phase change, and microstructure kinetics of phase change. III, J. Chem. Phys. (1941). https://doi.org/10.1063/1.1750872.

[21] W. Dietz, Sphärolithwachstum in Polymeren, Colloid Polym. Sci. 259 (1981) 413–429. https://doi.org/10.1007/BF01524878.

[22] H. Shan, G.C. Lickfield, Crystallization Kinetics Study of Polyethylene, Int. J. Polym. Anal. Charact. 12 (2007) 327–338. https://doi.org/10.1080/10236660701355345.

[23] J.E. Dutrizac, The reaction of sulphur vapour with molybdenum metal, Can. Metall. Q. 9 (1970) 449–453. https://doi.org/10.1179/cmq.1970.9.3.449.

[24] M. Bolhuis, J. Hernandez-Rueda, S.E. van Heijst, M. Tinoco Rivas, L. Kuipers, S. Conesa-Boj, Vertically-oriented MoS_2 nanosheets for nonlinear optical devices, Nanoscale. 12 (2020) 10491–10497. https://doi.org/10.1039/D0NR00755B.

[25] C. Albano, J. Papa, M. Ichazo, J. González, C. Ustariz, Application of different macrokinetic models to the isothermal crystallization of PP/talc blends, Compos. Struct. 62 (2003) 291–302. https://doi.org/10.1016/j.compstruct.2003.09.028.

[26] A. Splendiani, L. Sun, Y. Zhang, T. Li, J. Kim, C.-Y. Chim, G. Galli, F. Wang, Emerging Photoluminescence in Monolayer MoS_2, Nano Lett. 10 (2010) 1271–1275. https://doi.org/10.1021/nl903868w.

[27] J. V. Pondick, J.M. Woods, J. Xing, Y. Zhou, J.J. Cha, Stepwise Sulfurization from MoO_3 to MoS_2 via Chemical Vapor Deposition, ACS Appl. Nano Mater. 1 (2018) 5655–5661. https://doi.org/10.1021/acsanm.8b01266.